Full-Time, Eye-Safe Cloud and Aerosol Lidar Observation at Atmospheric Radiation Measurement Program Sites: Instruments and Data Analysis

James R. Campbell, [*] Dennis L. Hlavka, [*] Ellsworth J. Welton, [**] Connor J. Flynn, [***] David D. Turner, [***] James D. Spinhirne, [+] V. Stanley Scott, III [+], I.H. Hwang [×]

[*] *Science Systems and Applications, Inc., Lanham, Maryland*

[**] *University of Maryland, Baltimore County*

[***] *Pacific Northwest National Laboratories, Richland, Washington*

[+] *NASA Goddard Space Flight Center, Mesoscale and Atmospheric Processes Branch, Greenbelt, Maryland*

[×] *Science and Engineering Services, Inc., Burtonsville, Maryland*

[*] *Corresponding author address:* James R. Campbell, c/o Code 912, NASA/Goddard Space Flight Center, Greenbelt, MD, 20708. E-mail: campbell@virl.gsfc.nasa.gov

ABSTRACT

Atmospheric radiative forcing, surface radiation budget, and top of the atmosphere radiance interpretation involves a knowledge of the vertical height structure of overlying cloud and aerosol layers. During the last decade, the U.S. Department of Energy through the Atmospheric Radiation Measurement (ARM) program, has constructed four long-term atmospheric observing sites in strategic climate regimes (north central Oklahoma, Barrow, Alaska, and Nauru and Manus Islands in the tropical western Pacific). Micro Pulse Lidar (MPL) systems provide continuous, autonomous observation of all significant atmospheric cloud and aerosol at each of the central ARM facilities. Systems are compact and transmitted pulses are eye-safe. Eye-safety is achieved by expanding relatively low-powered outgoing pulse energy through a shared, coaxial transmit/receive telescope. ARM MPL system specifications, and specific unit optical designs are discussed. Data normalization and calibration techniques are presented. A multiple cloud boundary detection algorithm is also described. These techniques in tandem represent an operational value added processing package used to produce normalized data products for cloud and aerosol research and the historical ARM data archive.

1. Introduction

The success, or failure, of global numerical climate simulations can be traced directly to the accuracy of the empirical relationships and input parameters required to replicate significant dynamic and radiative processes. Knowledge of the vertical structure of cloud and aerosol scattering from varying climate regimes is fundamental. Analysis of surface or top of the atmosphere radiative fluxes is not sufficient in itself. Models that can correctly define these fluxes may have erroneous heating and cooling rates embedded within the atmosphere. There are numerous variables and measurements required in order to fully understand the radiative impact of cloud and aerosols, but accurate measurements of occurrence, height and thickness are relatively sparse. Deficiencies in essential global observations combined with increasing anxiety surrounding the impact of fossil fuel consumption and various other human activities on the atmosphere are the focus of a great deal of ongoing research (e.g. Wielicki et al. 1995).

The Atmospheric Radiation Measurement (ARM) program marks one of the key components of the strategy of the U.S. Department of Energy to address cloud and aerosol research. The ARM philosophy (Stokes and Schwartz 1994) is to gather time-extended measurements from several locales by creating and operating long-term observing sites equipped with diverse arrays of passive and active remote sensing, as well as in-situ instrumentation. Four such sites have so far been established, representing three distinct regions: mid-latitude continental (north central Oklahoma – SGP), tropical (Manus and Nauru Islands – TWP-M and TWP-N respectively) and polar (Barrow, Alaska – NSA) regimes.

The direct detection of atmospheric cloud and aerosol generally involves active-based remote sensing techniques, such as radar and lidar. Lidar systems are particularly sensitive to smaller atmospheric particles due to their enhanced scattering at visible wavelengths (Sassen 1995). However, continuously running lidars (necessary for the full-time requirements of climate measurements) are a fairly recent development and represent a significant departure from traditional application. Costs combined with a maintenance-intensive nature have historically limited widespread lidar usage (Sassen 1991). Limited lifetimes and safety considerations arising from high energy output are additional drawbacks. The Micro Pulse Lidar (MPL), developed in 1992 at NASA/Goddard Space Flight Center (GSFC) (Spinhirne 1993) overcomes many such common obstacles. MPL instruments are a long-standing member of the ARM instrument suite. The MPL technology applies advances in solid-state, diode-pumped lasers with appreciable operational lifetimes, and the introduction of high-efficiency quantum noise-limited photon counting devices. The most notable MPL feature is that its transmitted energy pulses are eye-safe. Low pulse energies (microjoules -- standard lidars are routinely orders of magnitude higher) are expanded through a shared Cassegrain transmitter/receiver (transceiver) telescope at a high repetition rate (2500 Hz). This eliminates the common safety requirement of supervised instrument operation and makes operation autonomous.

MPL data are processed for standard products including the heights of cloud layers and the vertical distribution of optical scattering cross sections. Processed datasets and results are disseminated to the atmospheric research community through the ARM program. For users of MPL data a reference for instrument function and calibration, and data retrieval

methods is necessary. In this paper we describe the MPL instruments and their use at ARM sites. We further describe the nature of measured raw signal and its normalization process. An operational cloud boundary height algorithm is also described.

2. Instrument

MPL instruments detect all significant tropospheric cloud and aerosol, to the limit of signal attenuation, through appreciable pulse summation and geometric signal compression (Spinhirne 1995). Additionally, a narrow receiver field-of-view (approximately 100 μrad) eliminates complications from multiple scattering, and limits the effects of ambient solar background. The MPL package is rugged and compact allowing for simple deployment and operation (given a temperature-controlled and weatherproof shelter). Systems have been demonstrated to run continuously for a period on the order of one year before requiring major maintenance. Aside from basic measurements of cloud boundaries, MPL data can be used to calculate cloud scattering cross sections and optical thicknesses, planetary boundary layer heights and aerosol extinction and optical thickness profiles, including those into the stratosphere in nighttime cases (Spinhirne 1993, Welton et al. 2000).

Table 1 notes the dates of operation, relevant diagnostic capabilities and settings for the historical and current ARM MPL units. Measurements at SGP began in December 1993, TWP-M in February 1997, NSA in March 1998, and TWP-N in November 1998. Specific revisions have been made to the MPL breadboard design described by Spinhirne (1993), as units began commercial production and distribution through Science and Engineering Systems, Inc. (SESI) of Burtonsville, MD. Over 20 MPL systems have since entered the community. Accounting for optical upgrades and improved data acquisition

rates, four different versions of the MPL have been used among the seven historical ARM systems.

ARM sites house large numbers of instruments, and they are typically remote in nature (raising the issue of timely maintenance initiative). Instrument simplicity and practicality therefore becomes a valuable asset. Both of these characteristics figure prominently in the design of MPL. Eye-safety permits autonomous system operation without concern for user or bystander safety. It also indirectly contributes to a manageable package size. The singular transceiver design, required to expand outgoing pulse energies to make the beam eye-safe, allows for a much smaller system compared to the more commonly used separate transmit/receive lidar optical design. Displayed in Fig. 1a and b are two versions of the MPL housing respectively along side a multi-channel scalar unit, laser power supply and operating computer. The configuration in Fig. 1a (henceforth referred to as V1.0) was used through the first four ARM units (00, 02, 03, and 54). A schematic drawing of V1.0 can be found in S95. The base container (approx. 40x40x20 cm^3) houses all optical components, which are mounted mostly along the inside of its top panel. The transceiver is fastened atop the outside of this upper plate, with external cable connections accommodated along a backside plate. While particularly stable, V1.0 proved somewhat bulky and lacked a simple means for operating at non-zenith viewing angles. These concerns were addressed in the upgraded tubular casing design shown in Fig. 1b (V2.0). V2.0 is the model used for the most recent ARM deployed instruments (units 58, 59 and 72). The base optics box is replaced by two mounting plates: a 30 cm long piece affixed slightly off of the 22 cm diameter axis of the telescope bottom extending out behind it, and a circular base plate attached perpendicular to the former at

its end. The connected segment is covered with an aluminum cylinder. Optical components are fastened along the extension plate, while external interfaces are handled along the back face. Pivoting rings fix the unit within two stanchions and a foundation plate allowing the transceiver to pivot over variable viewing angles, adjustable manually as desired. A tightening screw within the pivots adjusts the rigidity of the mount, thus fastening the unit in place at a desired viewing angle. Optical calibration of the system is made easier by simple manipulation of this angle (to be discussed). Total package volume for both system versions total well below 1 m^3. The compact size and construction makes the MPL easily portable, and increases its ruggedness and durability.

The MPL lasers are a diode-pumped Spectra Physics 7300-L3 Nd:YLF model, with 7960-L3 short cavity head (1047 nm, 1.0 W) and 7965-L3 frequency doubler module (523 nm). The laser diode rests in the laser power supply container, and is fiber-coupled externally to the head. An advantage of these lasers is the capability for variable pulse repetition frequencies (PRF) accomplished through an acousto-optic q-switching mechanism. For standard operation, the MPL PRF is set to 2.5 kHz. At this rate approximately 20 μj per pulse exits the laser aperture. The pulse length is less than 10 nsec, and beam divergence at this point is approximately 1.2 mrad, half-angle. The detector is an actively quenched EG&G SPCM-AQ-100 Geiger mode avalanche photo diode (GAPD) photon counting module. Quantum efficiencies approach 70% and maximum count rates near 20 MHz for these solid-state devices.

The 'shared' MPL optical paths coincide through a 20 cm aperture, adjustable focal length Celestron-made Schmidt-Cassegrain telescope. Early experiments with a co-axial MPL indicated that maintaining a transmit-receive alignment was extremely difficult due

to the very small field-of-view. With a common telescope and field stop alignment stability is much less of a problem. Also finding the 'boresight' is reduced from technically damaging operation to the simplicity of sending the transmit pulse to the receiver field stop. An outline of the initial standard MPL optical design and a simple ray-trace is shown in Fig. 2. With one exception (to be discussed), V1.0 and V2.0 share the same layout. Each pulse is turned from the separated laser path to the shared path by a combination angled mirror and polarized beam-splitting cube (V1.0) or thin-film polarizer (V2.0). A positive lens then focuses the beam down to the telescope focal point. A 200 μm pinhole is placed here representing the system field stop (i.e. field-of-view limiting aperture). A pseudo-random depolarizing cube placed beyond the focal point is the last component a pulse interacts with before being collimated by the 20 cm diameter telescope. Ideally the outgoing pulse divergence is diffraction-limited to approximately 35 μrad. However, inevitable blurring causes the measured value to be more on the order of 50 μrad. Transmission efficiencies through the exit path are on the order of 40%. Outgoing transmitted pulse energies average around 6-8 μj. which is well within the 25 μj ANSI eye-safety threshold quoted for a 20 cm aperture source.

Along the receive path, the telescope focal length is set to approximately 1.7 m. Given the field stop diameter, the receiver field-of-view is approximately 120 μrad. Laboratory measurements demonstrate its effective value to be more on the order of 100 μrad. This extremely narrow field of view eliminates the known ambiguities associated with the multiple scattering of the lidar signal (Eloranta 1998), and limits detection of ambient background light. The positive lens behind the pinhole collimates the randomly polarized backscatter, before it passes through the beam-splitter device to the separated

receive path. Two narrow interference filters (approx. 1.2 Å combined spectral width) are placed in front of a final positive lens that focuses energy down onto the detector.

Along the shared portion of the optical axis, an outgoing pulse interacts with four reflective surfaces; the positive lens in front of the pinhole, the outer edges of the pinhole itself, the random depolarizer, and the telescope corrector plate. Backward reflections from these surfaces inadvertently reach the detector at the onset of each sampling period as triggered by the laser pulse. The significance of this energy is enough to momentarily (approx. 200 ns) saturate the GAPD. The saturation is found to generate a run-on signal that decays gradually through the length of the sampling period. This so-called 'afterpulse' is of appreciable magnitude and data post-processing must account for it. This point will be examined further in Section 3b. Laboratory measurements have shown that scatter off of the pinhole contributes significantly to the internal reflections. Therefore, the focus of the detector relative to the pinhole is shifted slightly in the final alignment stages such that the system exit pupil (image of the primary mirror of the telescope) is imaged onto the detector rather than that of the pinhole. However, the size of this image is larger relative to that of the pinhole. It can potentially be larger than the active surface area of the GAPD. In such cases the detector active area is overfilled such that this point becomes the actual system field stop. The receiver field-of-view narrows slightly in such cases.

A alternate optical configuration can be used to limit the effects of afterpulsing. This design decreases the number of reflective surfaces an outgoing pulse interacts with. The pinhole and its corresponding positive/collimating lens are retracted behind the shared path coaxial junction. The pulse still interacts with the telescope corrector plate and

random depolarizer, but their contribution to afterpulsing is of much less significance. Figure 3 details the design scheme. The modification requires an increase in the telescope focal length (now approx. 2.0 m) to accommodate the retracted spacing of the pinhole. The receiver field of view at the pinhole then decreases to 100 μrad, though laboratory measurements have found the effective value to be ~ 90 μrad. The system focal point must now be set twice (once along each path). Along the outgoing path, a negative lens is used, placed just after the turning mirror but before the path junction. A beam-splitting cube is used to turn the beam towards the depolarizer and telescope. The pinhole/positive lens combination rests behind the cube, translating all incoming light to the filters and detector as discussed earlier. As these modifications are logistically rather simple, V2.0 systems can be upgraded with relatively minor effort. As of November 2000 one ARM unit featured this upgrade (unit no. 72, which we'll now term V2.1). Additional systems are in the process of being upgraded. A comparison of afterpulsing between a V2.0 and V2.1 system is displayed in Fig. 4. V2.1 modifications lower the effect significantly by roughly an order of magnitude.

The MPL data system consists of an SESI-manufactured multi-channel scalar card (MCS) package, connected through a serial cable to the detector. Its output is then read through a National Instruments PC-DIO-24 data acquisition card and serial cable by a Windows-based software package run by a PC laptop computer. Two versions of the MCS have existed among the ARM units. The first version allowed static range sampling periods of 2 μsec (300 m vertical resolution) and is no longer used. An updated model allows for user-variable settings of 300, 150, 75 and 30 m maximum as regulated through the software interface. ARM systems equipped with this MCS typically use the

maximum 30 m setting. The first three ARM systems (00, 02 and 03) were originally equipped with the low-resolution MCS. The last three (54, 58, 59 and 72) feature the updated model (note that the rather arcane numbering scheme of the systems depends on this feature as higher resolution systems simply have a value of 50 added to their original unit number). At 2.5 kHz, there is 400 μs between consecutive pulses allowing a maximum of 60 km of data to be recorded. A software interface setting allows the user to decide how much of this data is to be saved to the raw output file. This option becomes important when calculating the amount of ambient background counts persisting during a shot sample, which will be explained further in section 3c. S93 showed that pulse summation is required to reach appreciable signal-to-noise ratios given the low outgoing pulse energies. A software setting allows the user to determine the sample-averaging interval by which photon counts per range bin are stored in the data file. ARM systems have been set to either 30 or 60s. The MCS relays temperature readings from three thermistors mounted inside the optics canister. Voltage readings from an energy monitor mounted in front of the laser aperture are transmitted, and converted to μj using a look-up table calibrated for each system. Height-sampling period-intensity readings are displayed in real-time on the PC screen along with system diagnostics.

3. Data Processing

Temporally and spatially averaged photon counts (to be referred to simply as "shots") are written to the local storage disk in a simple GSFC-developed binary format concatenated into hourly files. Though software has been developed within the ARM project to simultaneously rewrite these data into the more flexible, and arguably more

efficient netCDF format (C. J. Flynn and B. Ermold, 1998, personal communications), we concentrate here on the original structure as it pertains to the system software package directly. A header precedes each shot profile denoting significant system settings (discussed previously) and relevant housekeeping details (e.g. time stamp, energy monitor, component temperatures, etc.) with sum byte size varying by system version. The prototype (unit no. 00) used a 25 byte header, subsequent low resolution MCS (henceforth referred to as LR) systems use 36 bytes and high resolution (HR) systems employ 44. Following the header, shots are broken into range-resolved raw counts via successive four byte segments taking the form:

$$n(r) = \frac{b(1)*256^3 + b(2)*256^2 + b(3)*256 + b(4)}{1.0x10^8} \qquad \textbf{(1)}$$

With the effective sampling range set to the maximum 60 km LR systems can inspect as many as 200 range bins (800 bytes), while HR systems sample a maximum of 2001 (8004 bytes). A complete day of LR data using 60 s sample averaging totals nearly 1.2 MB of data, while corresponding HR systems record slightly over ten times this amount. While interest lies mainly in signal measured (pointed vertically) from the first 20 km, sampling out to the maximum 60 km (as all ARM systems do) serves to measure background counts, which will be discussed below.

At the SGP and NSA sites, raw files are uploaded hourly to central servers. Data recorded at the TWP sites are backed-up onto tapes, and delivered to ARM when

possible. The ARM Data Center is responsible for data ingest, and also manages its storage, dissemination to data users, and post-processing.

From the lidar equation, MPL raw counts take the form:

$$n(r') = \frac{\left(\frac{O_c(r')CE\beta(r')T(r')^2}{r'^2}\right) + n_b + n_{ap}(r')}{D[n(r')]} \qquad (2)$$

where n equals the measured signal return in photo electron counts per second at range r′, O_c is the overlap correction as a function of range caused by field-of-view conflicts in the transceiver system, C represents a dimensional system calibration constant, E is the transmitted laser pulse energy, β is the backscatter cross section due to all types of atmospheric scattering, T is atmospheric transmittance, n_b is background contribution from ambient light, n_{ap} is the contribution from afterpulse, and D is the detector photon-coincidence deadtime as a function of raw count rate. Note that range is written in the initial form r′ to account for the sum of two offsets (Δr_o) such that:

$$r = r' - \Delta r_O \qquad (3)$$

where r is the actual range. The first portion of this offset results from the software recording range being the temporal distance to the end of a sampling bin. To maintain consistency with other ARM cloud profilers this value is modified to represent the bin center (E.E. Clothiaux and D.D. Turner, 1999, personal communication), requiring a

subtraction equal to half of the system range resolution. The second portion of the offset accounts for a timing inaccuracy between the laser pulse and MCS triggers. LR systems have a negative offset such that the laser fires before photon counting begins while HR systems routinely fire afterwards (both vary slightly with system). A simple means of estimating the discrepancy is possible in HR data by examining counts per bin from a representative shot sample (~ 60 s) in 30 m resolution. The first bin where significant counts are present depicts the laser firing, and its range is the spatial offset. This value is routinely on the order of two such range bins, or 60 m (400 ns). LR systems could be calibrated quite as simply as their 300 m maximum resolution is much larger than the standard deviance. However, it has been measured in the laboratory to be roughly –120 m (- 800 ns).

Accounting for Eq. 3 in Eq. 2 and assorting the correction terms on the left side of the equation yields un-calibrated MPL normalized relative backscatter (NRB):

$$\frac{\left[\left[n(r) * D[n(r)]\right] - n_{ap}(r) - n_{b}\right] r^{2}}{O_{c}(r) E} = C\beta(r) T(r)^{2} \qquad (4)$$

This value represents the baseline product of ARM value-added processing. Secondary algorithms, including cloud boundary detection and the calculation of significant optical parameters ingest this product as a starting point. Subsequent processing of NRB requires calculation of the system calibration constant (C). Solving for C cannot be done in real-time with a single-channel lidar alone. Welton et al. (2000) show that an

independent measurement of the vertical column aerosol optical depth offers the most practical means of solving C on a case-by-case basis.

Individual calibration terms break down as follows:

A. Deadtime -- ($D[n(r)]$)

The deadtime correction adjusts for the lower sampling frequency of the GAPD versus incident backscattered and ambient photon counts. Each detector has an explicit 'deadtime' period associated with recording a single photon avalanche event. Potential events during this time go undetected. A manufacturer look-up table is supplied with each unit providing the underestimate factor as a function of detector-reported counts per second. Such a relationship is plotted in Fig. 5. Detector deadtime for the EG&G SPCM is specified to be no higher than 60 ns, and actual performances are routinely half this amount. With relatively low transmitted pulse energies, observed count rates almost never reach the upper end of the detectors resolvable rate spectrum. In other words saturation via atmospheric scatter is rare. The linear-like region in Fig. 5, where correction values are on the order of 1, is most commonly applied.

B. Afterpulsing – ($n_{ap}[r]$)

Afterpulsing is an artificial signal profile induced by the initial laser pulse flash interacting with the GAPD. Internal system reflections saturate the detector diode at the beginning of a sampling period, and a very small leakage signal follow for a shot time period. (This situation is analogous to the human eye staring quickly at a bright object before blinking where brightness can still be sensed for a short period after the eye-lid is closed.) Charge dissipation is exponential-like amid the 400 μs sampling period between laser pulses. Figures 6a and c compare averaged profiles of deadtime and background-

corrected raw signal where the outgoing pulse was extinguished by a hard target immediately in front of the instrument (i.e. the remaining signal is now afterpulsing), versus similar profiles of clear-sky signal, for both V2.0 and V2.1 instruments. Figures 6b and d plot the percentage contribution to total count rates by the afterpulsing for each. It is clear that the contribution of afterpulse can be quite significant, particularly in the upper troposphere. When considering ARM datasets from the two TWP sites, where cirrus clouds are routinely found near the tropical tropopause to heights approaching 19 km, accurate afterpulse characterization is extremely important. Error estimates involving afterpulsing and its correction in data post-processing can be found in Welton et al. (2000).

Afterpulsing magnitudes vary as a function of system diagnostic variables. This includes ambient and internal temperatures, transmitted laser pulse energies, and background counts. In practice a relationship can't be directly derived. A method to determine an afterpulse function for a system is to operate in a 'blocked' configuration, producing a profile such as those in Fig. 6a and c. A correction can then be derived using a curve-fit or look-up table. Afterpulse calibrations for ARM systems are frequently done (approximately every month) to maintain accurate data post-processing. However, single, static corrections fail if the operating stability of the instrument is compromised such that afterpulsing magnitudes are fluctuating. Steps are taken to minimize this risk. First, ARM systems are operated in weather-sealed trailers where typical thermostat settings allow for no more than 2° C ambient variations at most. Internal system temperatures are therefore kept as stable as is generally possible. Second, the afterpulse correction is energy normalized so as to account for unavoidable changes in the amount of energy per

pulse (due to laser aging, dust, etc.). Equation 5 shows this where $n`_{ap}[r]$ represents the static correction as a function of range, E the shot-average energy monitor reading (μj), E_0 the average energy monitor reading for the profile used to calculate the correction file, and $n_{ap}[r]$ the final energy-normalized value:

$$n_{ap}[r] = n'_{ap}[r] * \frac{E}{E_0} \qquad (5)$$

Laboratory measurements have shown this scaling factor to be appropriate.

Blocked profiles used to derive the afterpulse calculation are best done when ambient background is not present. Past the blocking point, measured signal is the sum product of background, detector noise and afterpulse. Since background and afterpulse both represent unknowns, one must be eliminated to yield the other. This can be accomplished in a laboratory setting (i.e. a dark room when the system is pointed at a target) or more easily by applying a lid to the transceiver to eliminate background light. As detector noise rates are known, simply subtracting them from the count rates of each bin yields the afterpulse. It should be noted that initial detector saturation causes the GAPD to briefly paralyze after the initial laser pulse flash. Raw data collection in the near range is severely compromised by lingering ambiguities in the detector output for approximately 1.0 μs (150 m) while the GAPD stabilizes. Processed ARM HR data sets typically do not report data until 300 m (10 range bins) above ground level to overcome this. LR datasets are less susceptible due to their lower resolution and additional time offered by the laser/detector trigger offset.

C. Background – (n_b)

The narrow MPL receiver field-of-view greatly limits the amount of ambient background light incident upon the detector, however its magnitude remains of significance. ARM systems are exclusively operated while pointed vertically, such that past ~ 30 km it is presumed that no distinguishable backscatter is measured in the data. What is measured by the detector beyond this range is a combination of background, detector noise and afterpulsing. The latter value is adjusted first. Any representative sample of bins past 30 km can then be averaged to produce an estimate of the sum product of background and dark counts. For ARM post-processing, bins between 45 and 55 km are used. This limits the effects of potential error in the afterpulsing correction since its magnitudes are lowest towards the end of a sampling period. The MPL software package performs a similar calculation from bins between 50 to 60 km, storing the value in the shot data header. This particular range is not necessarily the most appropriate however. Due to the negative laser/MCS offset in LR systems (and potentially HR systems, though none have been seen as of yet), the end of a sampling period would occur after the laser pulse corresponding with the start of the following period thus contaminating a background measurement. For this reason, the 45 to 55 km range has historically been used to maintain consistency.

At the low latitude tropical sites, the MPL is run concurrently with a mechanical shutter mechanism. This apparatus shields the instruments for approximately one hour each day (ceasing data acquisition) when the sun approaches its daily maximum elevation

angle. The potential would otherwise exist for GAPD failure from extreme background count-rates as the solar disk nears the instrument field-of-view.

D. Overlap – ($O_c[r]$)

The near range overlap function is a well known factor for lidar signal. The narrow MPL receiver field-of-view (approx. 100 μrad) combined with the 20 cm transmit-receive aperture (20 cm) creates a near-field signal vignetting scenario, whereby optical efficiency within a finite range away from the instrument is compromised. Two mechanisms are responsible. Figure 7 illustrates the first by considering opposing points along the ends of a two-dimensional cross-section of the MPL telescope primary mirror (the system pupil). Geometrically, factoring in an approximate divergence of the collimated outgoing laser pulse (50 μrad), opposing points will not "see" the entire image from a given range until an easily calculable distance (approx. 4.0 km at these settings). It is this range where the diverging field of view intersects the outer edge of the beam. Optically however, with the field stop set at the focal point of the transceiver, images in the telescopes relative near-field do not focus down precisely at this point. As a function of range, they focus to a point behind the pinhole with variable image magnification size. This scenario is depicted in Fig. 8. The receiver field-of-view narrows, and again signal acquisition is compromised in response to vignetting of light from the greater diverging angles by the pinhole. The effects of this optical contribution to overlap linger for a range beyond the geometric point of unity. Typically, V1.0 and V2.0 systems achieve complete overlap just past 5.0 km. The effect in V2.1 systems increases slightly (to approximately

6.0 km) in response to the increased focal length of the telescope, and more narrow field-of-view.

Measures (1984) gives a complete treatment of the overlap function, and develops an equation for calculating the overlap range accounting for both vignetting scenarios. In practice an accurate calculation from optical parameters is not practical. Calibrating ARM systems for overlap, as a function of range, is solved for using a method described by Sasano et al. (1979). The starting point is an averaged data sample where the system is pointed horizontally with no obscuration. By choosing a time where the atmosphere is well-mixed such as late afternoon, or even better when aerosol loading is negligible, backscatter through the layer is roughly assumed to be constant with range (i.e., target layer is assumed homogeneous). Implicitly at some range r_o overlap is complete and the correction factor become 1.0. Equation (4) can be written as:

$$P(r) = \left[(n(r) * DTC[n(r)]) - n_b - n_{ap}(r)\right] * \frac{r^2}{E} = O_c(r) C\beta(r) T(r)^2 \qquad \textbf{(6)}$$

Knowing that $T(r) = e^{-\tau}$ and $\tau = \sigma r$, where τ is the optical thickness through the layer and σ is the extinction cross section, (6) can be rewritten as:

$$P(r) = O_c(r) C\beta(r) e^{-2r\sigma} \qquad \textbf{(7)}$$

For the section of this function where $r > r_o$ and $O_c = 1.0$ taking the natural log of both sides of (7) yields:

$$\ln[P(r)] = \ln[C\beta(r)] - 2r\sigma \qquad (8)$$

Since the layer is presumed homogeneous the ln[Cβ(r)] term is constant, and plotting ln[P(r)] versus r takes the form of y = mx + b to the limit of signal attenuation with -2σ as the slope m (the solid line in Fig.). An example of this is plotted in Fig. 9. Fitting such a function to a non-limited region where $r > r_o$, the slope value (m) can be calculated yielding σ. The ln[Cβ(r)] term is simply $\ln^{-1}(b)$ (y-intercept term). These values can then be used to solve for $O_c(r)$ using (7) and are plotted as the hollow circles in Fig. 9:

$$O_c(r) = \frac{P(r)}{C\beta(r)e^{-2r\sigma}} \qquad (9)$$

4. Multiple Cloud Boundary Detection Algorithm

A basic application for the MPL data is to define the height of cloud boundaries. A multiple cloud boundary height (MCBH) detection algorithm developed at GSFC for ARM MPL data is described in this section. This technique was developed to complement NRB products when value-added processing of the ARM historical and real-time MPL data stream commenced in 1998. Clothiaux et al. (1998) described a similar automated algorithm for MPL cloud detection based upon a routine applied to millimeter wavelength cloud radar data. They also introduced the so-called Scott-Spinhirne

algorithm developed years earlier at GSFC to calculate cloud base heights using simple raw signal strength thresholding. While it may appear somewhat excessive to use multiple techniques to calculate a common parameter, Clothiaux et al. (2000) argue strongly for the value of multiple algorithm integration when applied to the ARM data stream. In fact, the output of the current algorithm is divided into two separate products bounded by variable levels of sensitivity. Because many clouds are tenuous with ill-defined boundaries extracting cloud boundaries from lidar data is not a trivial task. No algorithm technique is perfect. Future work will consider inherent strengths and weaknesses as they pertain to the ARM MPL cloud algorithms to consolidate output into a uniform product.

The basis of the current algorithm is bi-directional differencing of adjacent range bins from individual shots compared to a similarly analyzed clear-sky baseline profile. Differences between the two are then subjected to specific threshold requirements for cloud boundary identification. The input parameter to the algorithm is NRB as described by (4). Data for a given day are first broken into consecutive two-hour sampling periods. Each sample is examined twice. First, the period is analyzed to determine whether information can be used to establish a clear-sky baseline. Second, to search for cloud boundaries.

To establish the clear-sky baseline each shot in a sample is scrutinized for large bin-to-bin signal discontinuities where its rather obvious that cloud-induced backscatter is present. A running three-point sum of the derivative of the natural log of NRB is taken from the first data range bin through to the final one. The range of the final bin is site-dependent (10 km at NSA, 15 km at SGP and 20 km at the TWP sites). Any bin where

this three-point sum exceeds 1.0 is believed to be indicative of cloud. This process identifies those profiles almost certain not to contain cloud scatter within the sample period. If a minimum threshold of profiles exists within the period not believed to contain cloud (variable again by site) these individual shots are averaged to create a profile of clear-sky vertical signal structure. The baseline consists of averaged NRB signal and corresponding signal-to-noise ratio (SNR) for each range bin. SNR is obtained by reverting NRB back to raw count rates as follows:

$$SNR(r) = \frac{\frac{N(r)O_c(r)N_s E}{r^2}}{\sqrt{\frac{N(r)O_c(r)N_s E}{r^2} + B_s N_s}} \qquad \textbf{(10)}$$

where N is NRB as a function of range, N_s is the actual number of laser pulses in a temporal shot average (either 1.5 E+05 or 7.5 E+04 based on the system setting) and B_s is the ambient background count. The baseline is stored as a reference to the cloud boundary search portion of the algorithm. If a subsequent period satisfies the clear-sky threshold requirement, the baseline is updated to incorporate the latest clear-sky information. Additionally, as large variations in range-dependent signal structure can occur within the planetary boundary layer (BL) on time scales of only a few hours, the section of the baseline below 3 km can be updated irrespective of the remainder if the minimum non-cloudy standard is reached in its region. Therefore despite cases of prolonged high cloudiness the BL section of the baseline can be updated. If the BL is updated exclusively a linear bridge is calculated between the two sections to smooth out

any discontinuities in relative signal differencing which may occur. This would arise in cases where C as denoted by (4) is unstable.

After a data sample period has been examined for possible baseline updating, the cloud boundary search commences. Each shot in the sample is scrutinized versus the baseline for cloud structure. Figure 11 displays algorithm output for the first seven range bins (approx. 2.0 km) of an LR shot taken by at TWP-M. The first column refers to the height above ground of the center of the corresponding range bin and the second notes its NRB value. The third column is the percentage increase of NRB from the bin below to the subject bin, with the same calculation from the bin above to the subject bin listed below. The fourth column is the same process done, though for the baseline, and the fifth column is cumulative difference between the values. The next four columns show the same process for SNR values. Note that for the first and last bins in the vertical column sampling range the baseline value of NRB and SNR for each of these two bins is used to simulate a lower or higher bin (which either doesn't exist or isn't calculated by the algorithm). The final two columns in Fig. 11 contain cloud boundary markers and the direction that the signal spikes responsible for them were calculated. A spike calculated working upwards is considered indicative of a cloud base, and a spike calculated downwards is considered to represent cloud top. A spike is determined when there exists a single or two-bin cumulative relative NRB increase with respect to the baseline (either upward of downward) of at least 55%, and a corresponding SNR increase greater than 42% (the number is actually slightly less near the ground).

It follows from (10) that NRB and SNR are empirically entwined. That is, for a particular background count rate, a 55% increase in SNR is equal to a 42% increase in

SNR. But, because background rates fluctuate diurnally, this relationship is variable, and the cloud spike threshold varies accordingly. For example, during daylight hours where background values are relatively high, a 55% increase in NRB corresponds to an SNR increase of well over 42%. During nighttime hours, where background rates are very low, a 55% increase in NRB corresponds to a much lower SNR increase much less 42%. Therefore, the threshold is essentially elastic. In cases of high ambient noise the NRB increase threshold determines whether or not a spike is identified (as the SNR threshold is satisfied intuitively). In the opposite scenario, it is the SNR threshold that is in control. The advantage of this technique is that the stability of the threshold is essentially conserved. The 55/42 relationship was determined in the relatively neutral case of dusk where background counts where at their diurnal median.

Working upward from the lowest range bin from the example in Fig. 10, an upwards spike is immediately detected at 0.27 km. The NRB and SNR values for this bin satisfy both threshold requirements (167% and 54% increases respectively). The algorithm recognizes this bin as a cloud base. Once a cloud base has been determined, the algorithm then searches for a corresponding downwards spike indicative of cloud top. Such a spike is found in the third bin at 1.17 km based on the two-bin running sum starting with the adjacent range bin at 1.47 km. However, an additional downward spike is found in this latter bin (64% and 53%). The algorithm ignores the lower bin and labels cloud top at the upper one. The process continues until the entire profile has been analyzed. The algorithm searches for as many as five distinct cloud layers. To accommodate the more coarse resolution of older LR datasets, gaps between clouds of one range bin (i.e. 300 m) are smoothed such that a gap of two bins, or 600 m, is required

between a cloud top and new base. In HR datasets this two-bin standard is maintained. However, with the ten-fold increase in resolution came an increase in raw signal noise that the algorithm technique was unable to satisfactorily overcome. With HR datasets, algorithm output is generated after decreasing the system resolution to 90 m. Thus, 180 m of separation is required between to distinguish between nearly adjacent cloud layers.

After analyzing all available data for a day, MCBH output at this point is categorized and stored as the "sensitive" cloud mask. The final step is to apply a smoothing filter to these data to limit erroneous cloud observations inadvertently triggered by signal noise. The filter is a six-shot by three-range bin weighting scheme similar to that described by (Clothiaux et al. 1999). An example of the cloud masks produced by the MCBH algorithm is displayed in Fig. 11 from the TWP-N site on 18 July 1999. This example highlights the strengths of both cloud masks. NRB from 0 to 20 km is displayed in the top of the figure, followed by respective mask output plotted in the middle and lower portions. It is immediately evident how beneficial the robust filter routine is to cleaning up the raw output from the sensitive mask in the middle and upper troposphere. The latter does a functional job picking out significant signal structure, particularly in the upper troposphere where in this example exists an optically thin (judging from signal count rates) cirrus cloud up to as high as 16 km. Of course, it is clear that much of this signal structure is due to noise. It should be noted, however, that this case is somewhat unusual given the proximity of this instrument to the equator and the subsequently high background count rates it routinely measures. The robust filter is able to significantly eradicate many of the false positives to produce a much more accurate view of the cloud scene. The sensitive mask proves more reliable in the lower troposphere where SNR is

much higher. In this example, its output is invaluable in this region, as the robust cloud filter tends to eliminate many of the sporadic clouds forming in the top of the marine boundary layer (as evidenced in the NRB display). In addition, the temporal and spatial weighting is not necessarily appropriate in the BL as a small cumulus case, for example, can exist only for a small time period in the instrument field-of-view.

5. Discussion and Conclusions

The ARM MPL project is notable for two important achievements. One is the deployment of the first autonomous lidar instruments for full-time operation. Second, the ARM network array provides the first multi-site homogeneous lidar dataset within the community. The practicality of these instruments is derived from eye-safe operation, but low power and compact system size is also important. These features stem from a shared transmit/receive optical path not typically seen in traditional lidar design conflicts arise through this design. Detector afterpulsing and the near-range overlap function can offer varying degrees of difficulty to data post-processing if not properly characterized.

MPL instruments have been in operation at ARM sites for over seven year. During that time measures have been taken to insure routine instrument servicing and calibration in the field, and regularly scheduled intensive maintenance only possible in a lab environment. Common maintenance procedures focus on keeping the systems and their immediate environment dust-free. The transmitting window atop the site operating trailer requires particular attention as dust and other pollutants from the local surroundings contaminate the window surface thereby decreasing signal transmission rates. Instruments are nominally operated for a period on the order of a year before requiring

major servicing. The Spectra Physics 7300-L3 laser diode is specified to operate for 5000 hours (~ 7 months) at a full 1 A current draw before appreciable degradation to the output signal energy commences. This will improve with continuing advances to the technology. EG&G photon counting detectors in practice have maximum lifetimes on the order of two years.

Overlap and afterpulse calibrations are constantly monitored to insure data quality. Changes to the optical alignment due to vibration and other aging factors over the period of even a few months are inevitable and are accounted for. Changes to afterpulsing are more frequent as the integrity of the system optical path and diode-pumped laser pulse energies are subject to unavoidable fluctuations. Aside from routine examination of raw data files, ARM instrument mentors can monitor pertinent system diagnostics via the Internet. File and screen sharing software, such as Netopias Timbuktu for Windows, allow for remote manipulation of an MPL system computer. This feature is used with both the SGP and NSA units where adequate Internet connections exist.

In this paper the algorithm for normalized relative backscatter profiles and the detection of multiple cloud boundary heights are described. Value added processing of the ARM MPL data stream (available in near real-time and through the historical archive) is based on these methods. The NRB results are robust when the system calibration factors as described are properly maintained. Cloud boundary detection is highly sensitive and accurate. An algorithm by Welton et al. (2001) describes the next step in the data processing hierarchy that calculates various optical properties from significant atmospheric layers (cloud and aerosol). This routine should be operational within the ARM data processing fold by summer 2001, providing aerosol extinction cross-sections,

cloud and aerosol optical depths, and boundary layer heights. Potential data users are encouraged to contact ARM[1] to inquire about specific availability of any such processed datasets. Gaps may exist in some data streams due to the optical integrity of particular systems during their operation.

Study of cloud and aerosol, both for ARM and potentially similarly motivated global satellite monitoring programs, benefit from extended MPL observations. The vertical distribution of atmospheric constituents is an indirect and ambiguous measurement for passive remote sensors. The application of direct, autonomous lidar systems, as a complement to a collocated suite of passive sensors, brings forth a nearly complete vertical characterization of the radiative state of the atmosphere. The ARM MPL project has demonstrated the practicality of small, continuous running lidars as included among intensive remote sensing instrumentation arrays. The need to bring about routine lidar application, onto scales similar to its analogous counterpart radar, is evidenced by the growing emphasis on cirrus clouds and aerosols as important radiative modulators. Sassen and Campbell (2000) applied a 2200 hour mid-latitude ruby-lidar dataset to compile a cirrus cloud climatology at Salt Lake City, Utah over a ten year period and is perhaps the most definitive cloud climatology so far produced. In relation ARM MPL instruments compile 2200 hours of data in just over three months. The comparison demonstrates the abundant possibility for MPL datasets. As upgrades and modifications are made to the technology, particularly with regards to implementing dual-wavelength and polarization scattering capabilities, the potential offered by MPL systems is substantial.

[1] Information regarding the ARM program can be found via the World Wide Web at http://www.arm.gov/

Acknowledgments

MPL research at NASA/GSFC has been funded by DOE Interagency Agreement DE-AI01-92ER61367 as part of the ARM program, and through the NASA Radiation Sciences program. PNNL is operated by Battelle Memorial Institute for the U.S. Department of Energy under contract DE-AC06-76RLO 1830. The authors thank M. McGill of NASA/GSFC for many valuable discussions and input, and R. Perez for assistance overseeing the production and archiving of the ARM MPL data archive.

References

Clothiaux, E. E., G. G. Mace, T. P. Ackerman, T. J. Kane, J. D. Spinhirne, and V. S. Scott, 1998: An automated algorithm for detection of hydrometeor returns in micropulse lidar data. *J. Atmos. Oceanic Technol.*, **15**, 1035-1042.

Clothiaux, E. E., K. P. Moran, B. E. Martner, T. P. Ackerman, G. G. Mace, T. Uttal, J. H. Mather, K. B. Widener, M. A. Miller, and D. J. Rodriguez, 1999: The Atmospheric Radiation Measurement Program Cloud Radars: Operational Modes. *J. Atmos. Oceanic Technol.*, **16**, 819-827.

Clothiaux, E. E., T. P. Ackerman, G. G. Mace, K. P. Moran, R. T. Marchand, M. A. Miller, and B. E. Martner, 2000: Objective determination of cloud heights and radar reflectivities using a combination of active remote sensors at the ARM CART sites. *J. Appl. Meteorol.*, **39**, 645-665.

Eloranta, E. W., 1998: Practical model for the calculation of multiply scattered lidar returns. *Appl. Opt.*, **37**, 2464-2472

Measures, R. M., 1984: Laser remote sensing - fundamentals and applications. Wiley 1984 ISBN 0-89464-619-2 510 pp.

Sasano, Y., H. Shimizu, N. Takeuchi, and M. Okuda, 1979: Geometrical form factor in the laser radar equation: an experimental determination. *Appl. Opt.*, **18**, 3908-3910.

Sassen, K., 1991: The polarization lidar technique for cloud research: A review and current assessment. *Bull. Amer. Meteorol. Soc.*, **72,** 1848-1866.

Sassen, K., 1995: Lidar cloud research. *Rev. of Laser Eng.*, **23,** 148-153.

Sassen, K., and J. R. Campbell, 2001: A remote sensing midlatitude cirrus cloud climatology: I. Macrophysical and synoptic properties. *J. Atmos Sci.*, **58**, 481-496.

Spinhirne, J. D., 1993: Micro pulse lidar. *IEEE Trans. Geo. Rem. Sens.*, **31,** 48-55.

Spinhirne, J. D., J. A. R. Rall, and V. S. Scott, 1995: Compact eye safe lidar systems. *Rev. Laser Eng.*, **23**, 112-118.

Stokes, G. M., and S. E. Schwartz, 1994: The Atmospheric Radiation Measurement (ARM) Program: Programmatic background and design of the cloud and radiation testbed. *Bull. Amer. Meteorol. Soc.*, **75,** 1201-1221.

Welton, E. J., J. R. Campbell, J. D. Spinhirne, and V. S. Scott, 2001: Aerosol and cloud measurements using Micro Pulse Lidar systems. Submitted to *J. Atmos. Oceanic Technol.*

Wielicki, B. A., R. D. Cess, M. D. King, D. A. Randall, and E. F. Harrison, 1995: Mission to planet earth: Role of clouds and radiation in climate. *Bull. Amer. Meteorol. Soc.*, **76**, 2125-2153.

Table Captions

Table 1. A historical listing of all ARM MPL systems by site, including their dates of operations, optical configuration versions, and temporal and spatial resolution settings.

Figure Captions

Figure 1. MPL instrument casing versions on either side of the multi-channel scalar, laser power supply, and system laptop computer. On the left is the prototype design (V1.0), and the upgraded canister design (V2.0) is on the right.

Figure 2. Simplified 2-D outline of the MPL optical design for V1.0 and V2.0 systems (ARM unit numbers 00, 02, 03, 54, 58 and 59). On the laser/outgoing path each pulse encounters a turning mirror, beam-splitting device, positive lens, pinhole and random depolarizer before reaching the transceiver. Along the incoming path sits the random depolarizer, pinhole, collimating lens, beam-splitting device, narrow-band interference filter pair, positive lens and photon-counting detector.

Figure 3. Simplified 2-D outline of the MPL optical design for V2.1 systems (ARM unit number 72). On the laser/outgoing path each pulse encounters a turning mirror, negative lens, beam-splitting cube and random depolarizer before reaching the transceiver. Along the incoming/detector path sits the random depolarizer, beam-splitting cube, pinhole, collimating lens, narrow-band interference filter pair, positive lens and photon-counting detector.

Figure 4. A comparison of ten-minute averaged detector afterpulsing signal profiles (range proportional to time) from original (V1.0 and V2.0) and upgraded retracted pinhole (V2.1) optical configurations in 30 m range resolution.

Figure 5. Sample photon counting detector deadtime correction, as a function of incident photon count-rates.

Figure 6. Comparison of raw photon count-rates from total signal and afterpulsing within the troposphere for V1.0 and V2.0 (a) and V2.1 systems (c) in 300 m range resolution. Relative percentages of afterpulsing to total signal for each are shown in (b) and (d).

Figure 7. A simplified 2D sketch of the geometric contribution to overlap inherent to the MPL optical design. Shown is the 200 μm diameter pinhole and 20 cm diameter telescope primary mirror. The solid line is the normal to the primary mirror surface. The dashed line represents the field of view (angle α, approx. 100 μrad) dictated by the pinhole diameter/telescope focal length combination. The dashed/dotted line represents the divergence of the outgoing laser pulse (angle β, approx. 50 μrad) after expansion through the Schmidt-Cassegrain system. Full overlap occurs at a range (r_0) where opposing edges of the primary can 'see' the entire span of the transmitted beam spot. This occurs when the dashed line (field of view) eventually crosses the dashed/dotted line (diverging laser pulse) on the opposing side.

Figure 8. A simplified, quasi-3D sketch of the optical portion of overlap inherent to the MPL optical design. (a) For an image at infinity, and all incident rays are focused down by the telescope to its focal point (i.e. the pinhole). Images in the near-field (b) focus down behind the pinhole, with a spot-size magnification a function of range and the focal length setting of the Schmidt-Cassegrain telescope. The pinhole however, blocks many of these rays from reaching the image plane, particularly those from outer diverging angles relative to the system field of view. As range increases from the instrument, the image size gradually decreases until the point where vignetting ceases and overlap is reached.

Figure 9. The natural logarithm of range-corrected, background, deadtime, and afterpulse corrected MPL data where the system is pointed horizontally. Under well-mixed conditions (i.e. homogeneous target layer) past the point where overlap is achieved signal fall-off is linearly proportional to total incident extinction. In this case, overlap unity is reached at 5.40 km.

Figure 10. An example of the subject multiple cloud boundary height algorithm methodology. The algorithm searches for areas of large bin-to-bin signal deviance as compared to a clear-sky baseline signal profile. This search is done by range bin by differencing NRB and SNR from adjacent bins, both above and below, and evaluating the difference relative to the baseline versus thresholds. When the thresholds are met, the algorithm designates the bin as the cloud base (as found in the 0.27 km bin). The routine then searches for a corresponding area of deviance denoting the cloud top (as found in the 1.17 km bin).

Figure 11. Example of MCBH algorithm output at TWP-N for 18 July 1999. In the top of the figure NRB signal is displayed from 0 to 20 km with scaling found on the right. Sensitive cloud mask output is plotted in the middle, and robust cloud mask output is displayed in the grid below.

Site	Unit	Version	Dates	ΔY	ΔT
SGP	00	1.0	12/93 - 3/96	300 m	60s
	02	1.0	1/96 - 8/98	300 m	60s
	54	2.0	8/98 – 11/98	30 m	30s
			1/99 - present		
TWP-M	03	1.0	2/97 - 11/97	300 m	60s
			4/98 – 10/99		
	72	2.1	11/99 – present	30 m	30s
TWP-N	59	1.0	11/98 – 1/99	30 m	30s
			4/99 – 2/00		
			6/00 - present		
NSA	58	1.0	3/98 - present	30 m	30s

Table 1

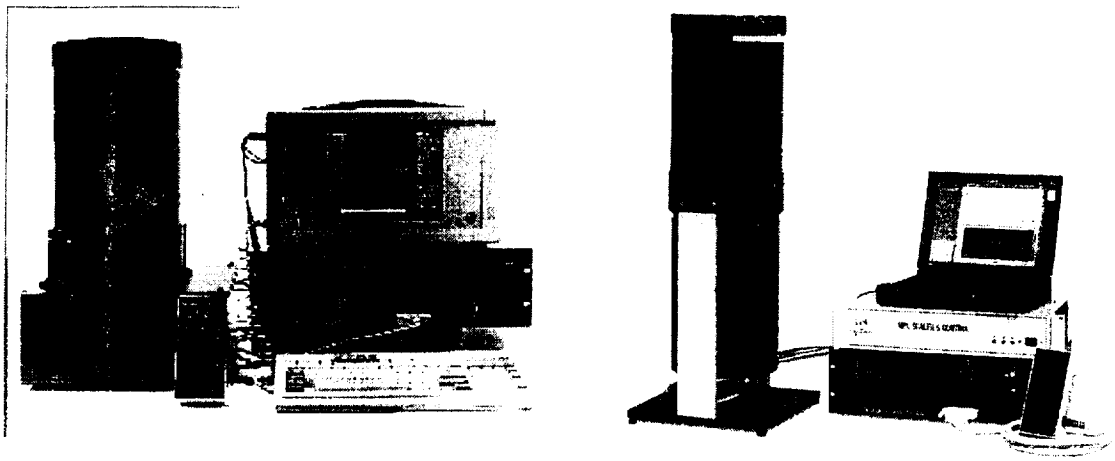

(a) (b)

Figure 1

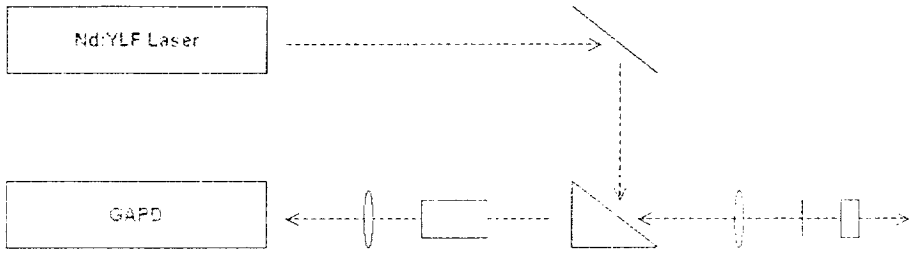

Figure 2

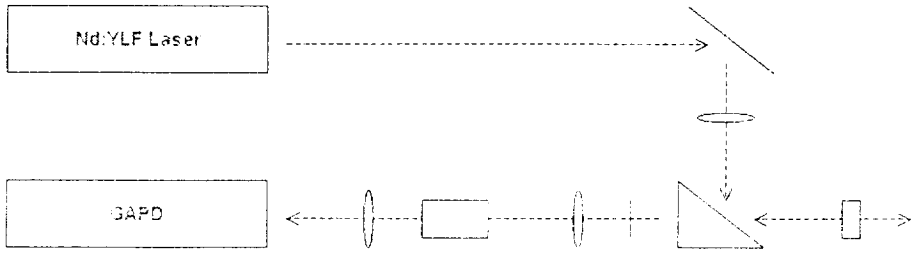

Figure 3

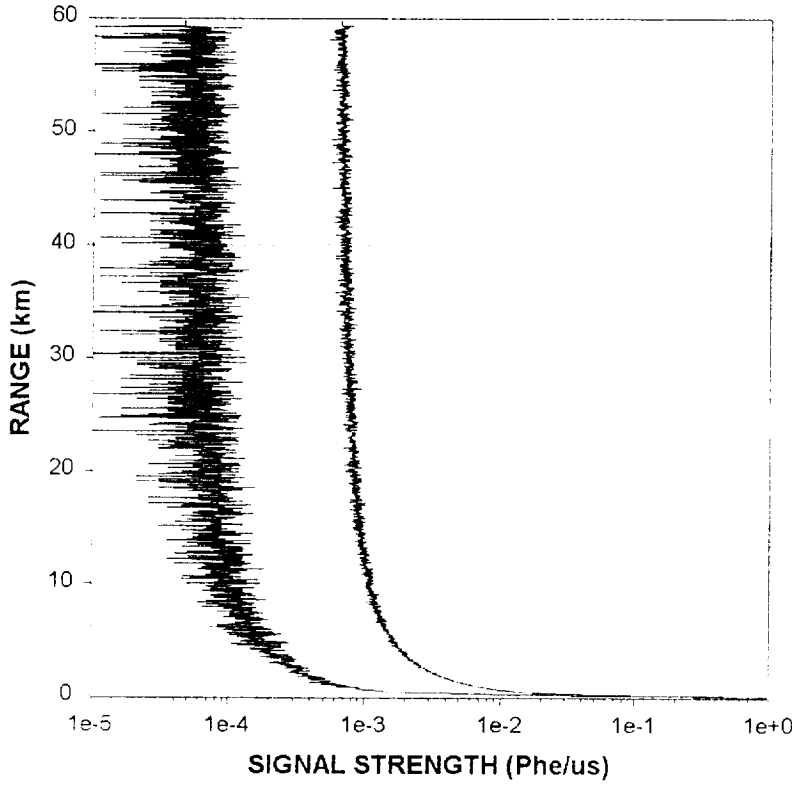
60
50
40
30
20
10
0
RANGE (km)
1e-5
1e-4
1e-3
1e-2
1e-1
1e+0
SIGNAL STRENGTH (Phe/us)

Figure 4

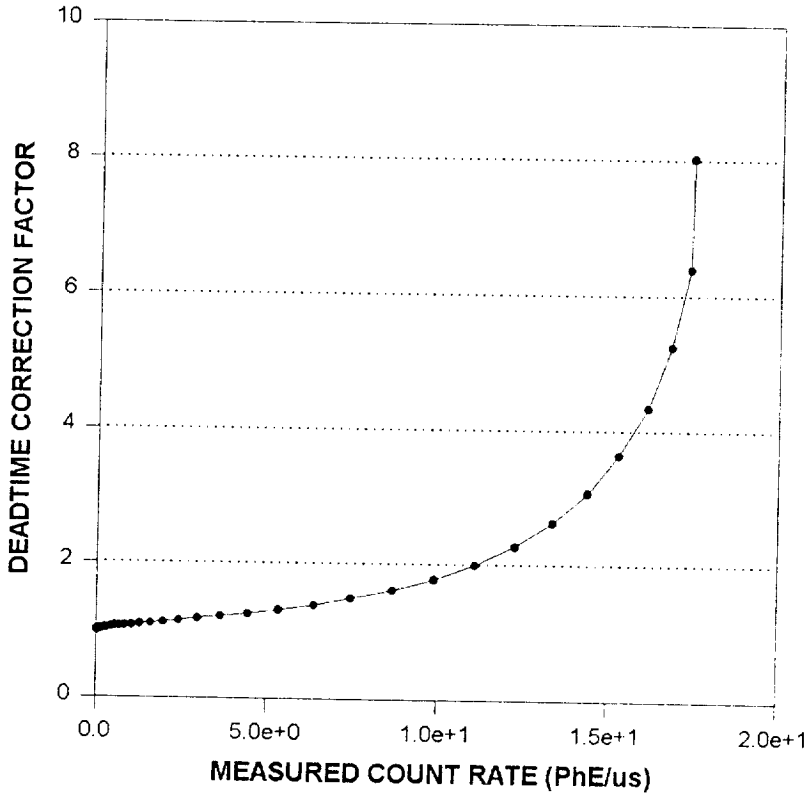
10
8
6
4
2
0
DEADTIME CORRECTION FACTOR
0.0
5.0e+0
1.0e+1
1.5e+1
2.0e+1
MEASURED COUNT RATE (PhE/us)

Figure 5

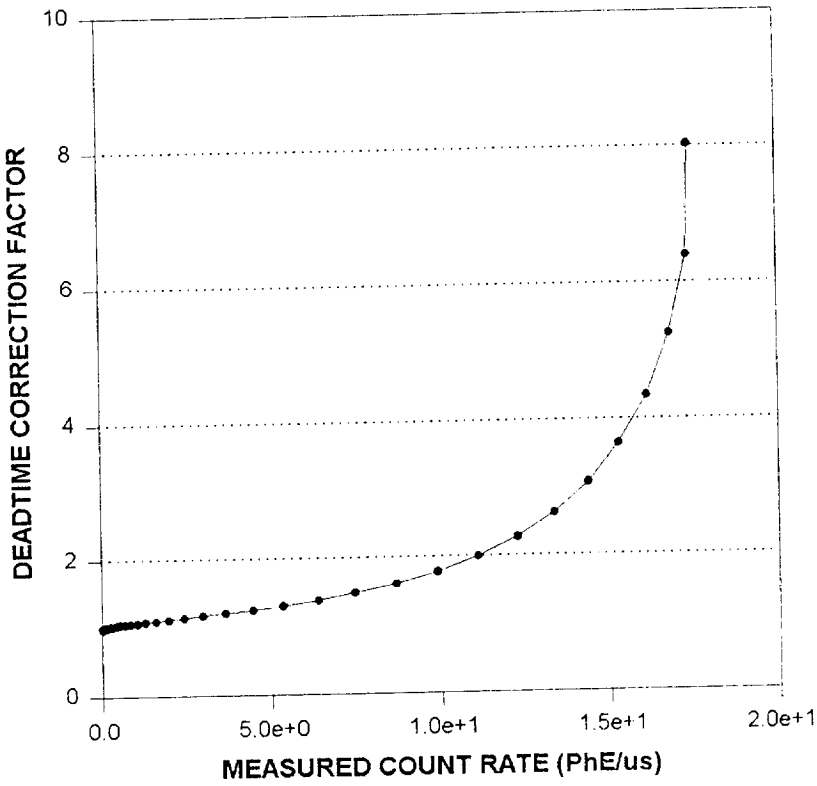
10
8
6
4
2
0
DEADTIME CORRECTION FACTOR
0.0
5.0e+0
1.0e+1
1.5e+1
2.0e+1
MEASURED COUNT RATE (PhE/us)

Figure 5

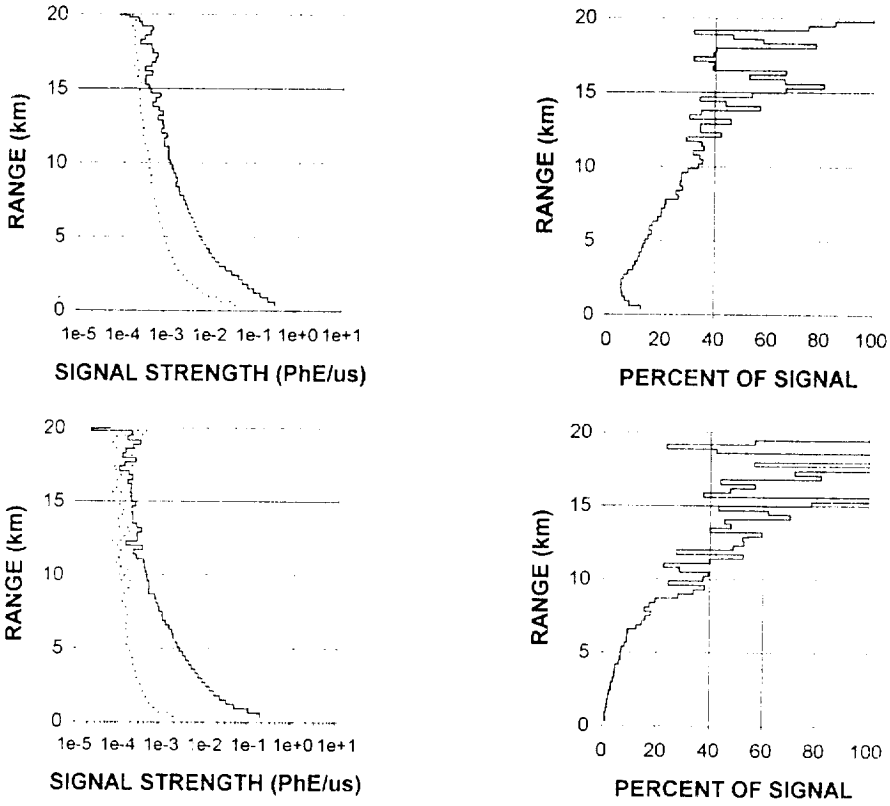
RANGE (km)
20
15
10
5
0
1e-5 1e-4 1e-3 1e-2 1e-1 1e+0 1e+1
SIGNAL STRENGTH (PhE/us)
RANGE (km)
0 20 40 60 80 100
PERCENT OF SIGNAL
RANGE (km)
1e-5 1e-4 1e-3 1e-2 1e-1 1e+0 1e+1
SIGNAL STRENGTH (PhE/us)
RANGE (km)
0 20 40 60 80 100
PERCENT OF SIGNAL

Figure 6

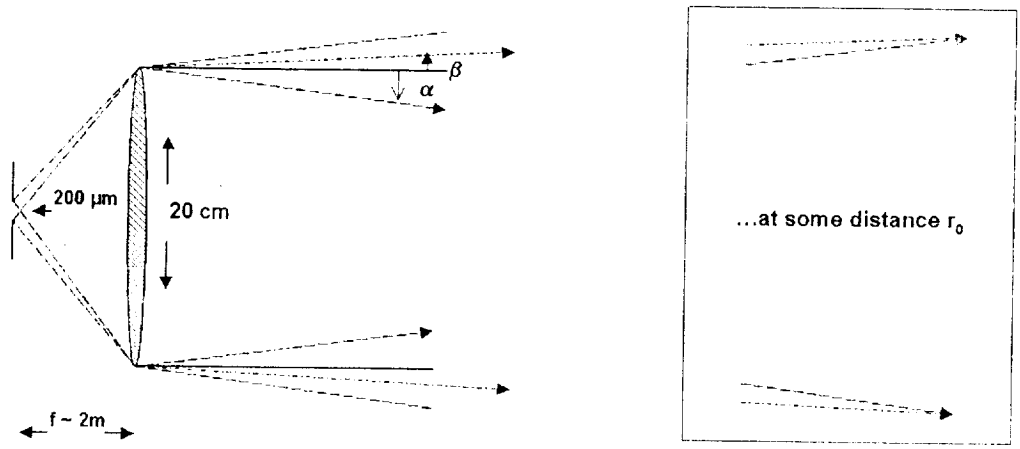

Figure 7

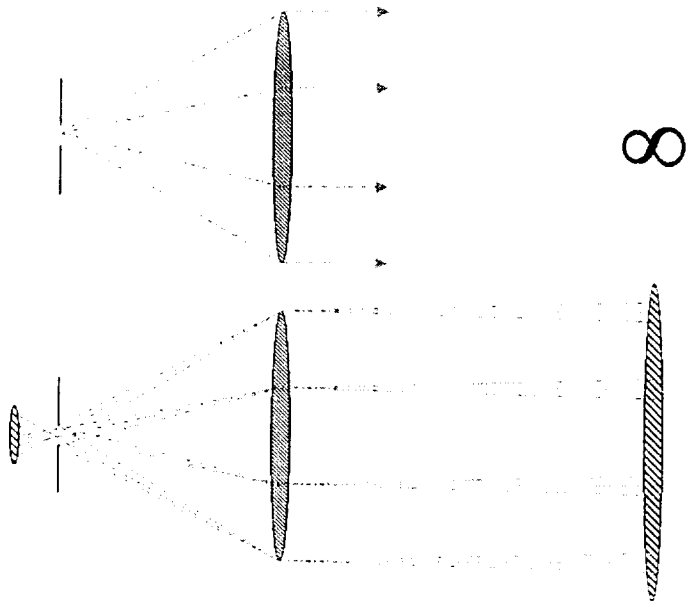

Figure 8

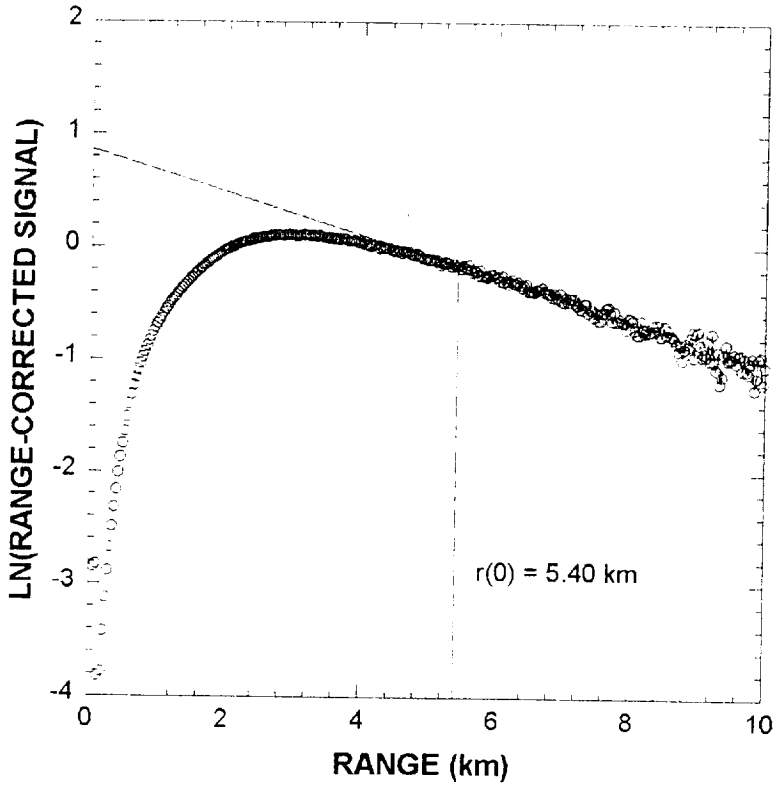
LN(RANGE-CORRECTED SIGNAL)
RANGE (km)
r(0) = 5.40 km
2
1
0
-1
-2
-3
-4
0
2
4
6
8
10

Figure 9

HGHT	BS	BSDF	BADF	DIFF	SNR	SNDF	BSND	DIFF	CLD	SPK
0.27	0.609	1.665	0	1.665	763.06	0.546	0	0.546	Base	yes
		-0.333	0.149	-0.481		0.261	0.605	-0.344		no
0.57	0.913	0.499	-0.129	0.628	605.04	-0.207	-0.377	0.17	Mid	yes
		-0.143	-0.037	-0.106		0.115	0.167	-0.053		no
0.87	1.065	0.167	0.039	0.128	542.79	-0.103	-0.143	0.04	Mid	no
		0.447	-0.043	0.49		0.503	0.132	0.371		yes
1.17	0.736	-0.309	0.045	-0.354	361.24	-0.334	-0.116	-0.218	Top	no
		0.591	-0.052	0.643		0.637	0.109	0.528		yes
1.47	0.462	-0.372	0.055	-0.426	220.72	-0.389	-0.098	-0.291	n/a	no
		0.351	0.018	0.333		0.489	0.138	0.351		no
1.77	0.342	-0.26	-0.018	-0.242	148.27	-0.328	-0.121	-0.207	n/a	no
		0.344	0.174	0.17		0.502	0.213	0.289		no
2.07	0.255	-0.256	-0.148	-0.108	98.71	-0.334	-0.176	-0.158	n/a	no
		0.247	0.34	-0.093		0.418	0.265	0.152		no

Figure 10

Figure 12

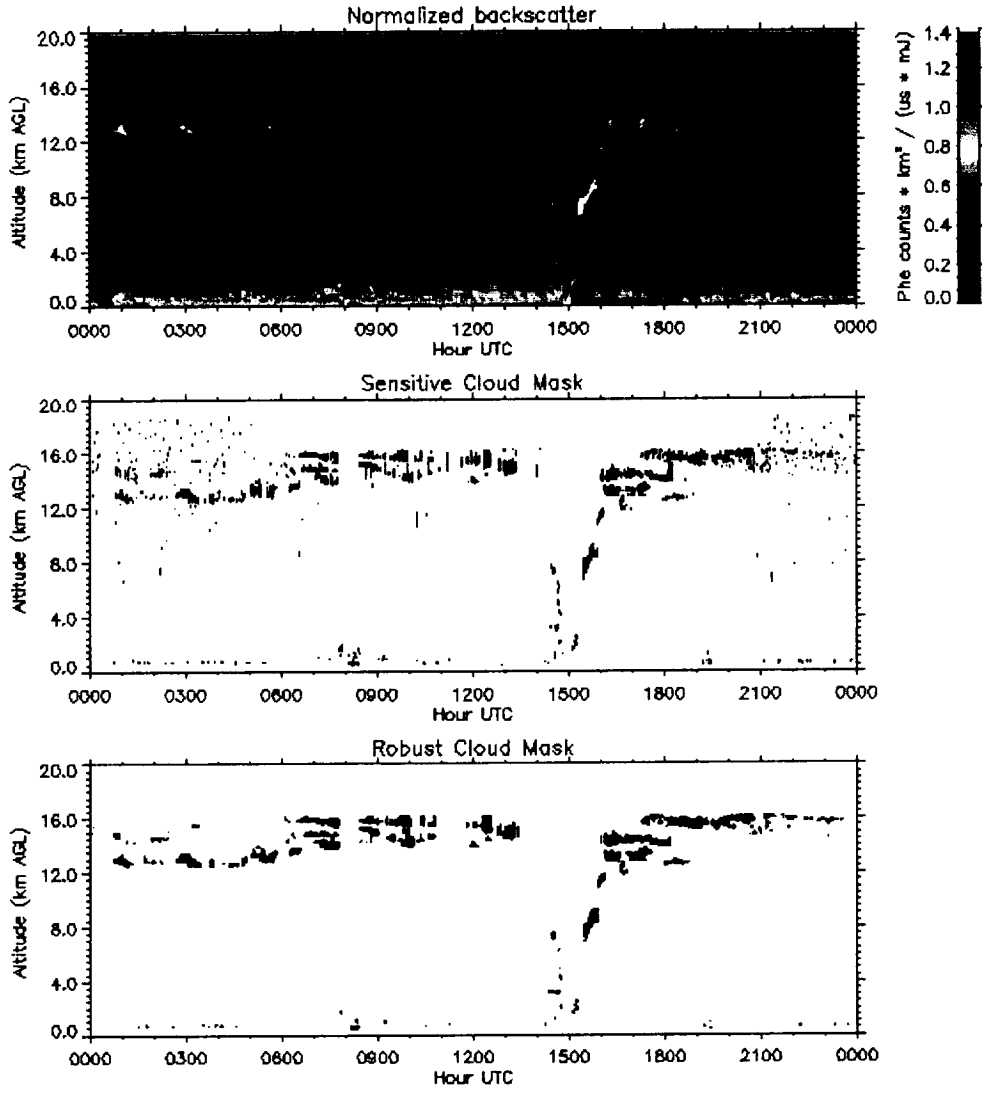
Normalized backscatter
Altitude (km AGL)
20.0
16.0
12.0
8.0
4.0
0.0
0000
0300
0600
0900
1200
1500
1800
2100
0000
Hour UTC
Phe counts * km² / (us * mJ)
1.4
1.2
1.0
0.8
0.6
0.4
0.2
0.0
Sensitive Cloud Mask
Altitude (km AGL)
Hour UTC
Robust Cloud Mask
Altitude (km AGL)
Hour UTC